J. Fluid Mech. (2010), *vol.* 663, *pp.* 456–477. © Cambridge University Press 2010
doi:10.1017/S0022112010003599

Three-dimensional flow evolution after a dam break

A. FERRARI[1]†, L. FRACCAROLLO[2], M. DUMBSER[1,2], E. F. TORO[2] AND A. ARMANINI[2]

[1]Institute of Aerodynamics and Gasdynamics, Pfaffenwaldring 21, D-70569 Stuttgart, Germany

[2]University of Trento, Via Mesiano, 77, I-38100 Trento, Italy

(Received 30 December 2009; revised 2 July 2010; accepted 3 July 2010;
first published online 12 October 2010)

In this paper, the wave propagation on a plane dry bottom after a dam break is analysed. Two mathematical models have been used and compared with each other for simulating such a dam-break scenario. First, the fully three-dimensional Navier–Stokes equations for a weakly compressible fluid have been solved using the new smooth particle hydrodynamics formulation, recently proposed by Ferrari *et al.* (*Comput. Fluids*, vol. 38, 2009, p. 1203). Second, the two-dimensional shallow water equations (SWEs) are solved using a third-order weighted essentially non-oscillatory finite-volume scheme. The numerical results are critically compared against the laboratory measurements provided by Fraccarollo & Toro (*J. Hydraul. Res.*, vol. 33, 1995, p. 843). The experimental data provide the temporal evolution of the pressure field, the water depth and the vertical velocity profile at 40 gauges, located in the reservoir and in front of the gate. Our analysis reveals the shortcomings of SWEs in the initial stages of the dam-break phenomenon in reproducing many important flow features of the unsteady free-surface flow: the shallow water model predicts a complex wave structure and a wavy evolution of local free-surface elevations in the reservoir that can be clearly identified to be only model artefacts. However, the quasi-incompressible Navier–Stokes model reproduces well the high gradients in the flow field and predicts the cycles of simultaneous rapid decreasing and frozen stages of the free surface in the tank along with the velocity oscillations. Asymptotically, i.e. for 'large times', the shallow water model and the weakly compressible Navier–Stokes model agree well with the experimental data, since the classical SWE assumptions are satisfied only at large times.

Key words: computational methods, hydraulics

1. Introduction

The purpose of this study is to reproduce a hypothetical scenario associated with extreme hydrologic events. Such overflow phenomena may result due to a dam collapse in an open valley. The main causes of rupture include spillway design error (South Fork Dam), geological instability caused by changes in water levels during filling or poor surveying (Vajont Dam, Malpasset), poor maintenance, especially of outlet pipes (Lawn Lake Dam, Val di Stava Dam collapse), extreme rainfall (Shakidor Dam) and

† Email address for correspondence: ferrari.angela@gmail.com

https://doi.org/10.1017/S0022112010003599 Published online by Cambridge University Press

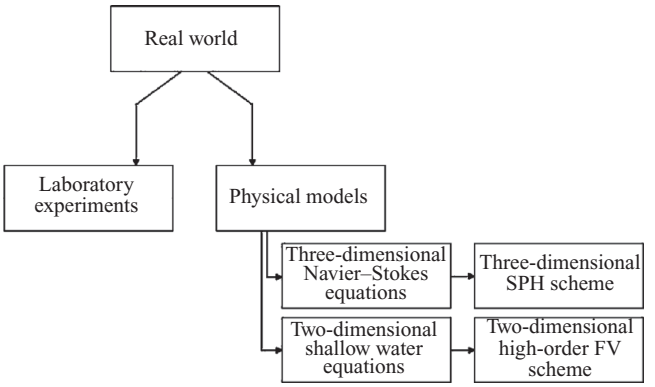


FIGURE 1. Sketch of the approach of this paper.

human, computer or design error (Buffalo Creek Flood, Dale Dike Reservoir, Taum Sauk pumped storage plant).

Experiments were carried out by Fraccarollo & Toro (1995) to reproduce a free-surface flood on a plane bottom after a dam break. The laboratory set-up provided measurements on the evolution of the water depth, the velocity distribution along the vertical direction and the pressure field at 40 gauges, located in the tank and in front of the gate.

Numerical simulations of inundation events also involving complex topography have become a wide research interest, thanks to the high rate of increase of computational power and their availability. In this paper, we do not discuss the causes of such extreme events, but the aim is to simulate the propagation of a flooding wave after a dam failure. Two mathematical models are used. First, we consider the complete hydrodynamics model of the weakly compressible Navier–Stokes equations derived from the first principles of conservation of mass, momentum and energy. They describe the time evolution of the physical and kinematic quantities of the fluid flow in space, along any direction. Instead of the Poisson relation, which is widely applied in the computational fluid dynamics, the Tait equation of state is used for the definition of the pressure in the Navier–Stokes equations. It was derived by Batchelor (1974), who reproduced the material rheology of weakly compressible fluids. The second model consists of the classical simplified approach given by the shallow water equations (SWEs), which is frequently applied in the framework of geophysical applications or hydraulic, civil or environmental engineering. The model is derived by depth averaging of the incompressible three-dimensional Navier–Stokes equations under the assumption that the characteristic horizontal length scale of the flow is much greater than the characteristic vertical length scale. This leads to neglect of any acceleration in the direction of gravity, resulting in a hydrostatic pressure distribution in water. Because of the depth-averaged integration, the governing partial differential equations (PDEs) are reduced to a two-dimensional system.

Figure 1 shows the conceptual scheme of the hierarchy of physical and mathematical models that we will consider in this paper. The laboratory experiments have been used to reproduce the real phenomena to a small scale. Observations and physical measurements can be taken to give a complete description of the phenomenon. The more complete model is given by the fully three-dimensional Navier–Stokes equations that are solved using the three-dimensional smooth particle hydrodynamics (SPH) scheme, recently proposed by Ferrari *et al.* (2009). The simplest and computationally

https://doi.org/10.1017/S0022112010003599 Published online by Cambridge University Press

least expensive approach consists of the SWE model solved using the third-order unstructured weighted essentially non-oscillatory (WENO) finite-volume (FV) scheme of Dumbser *et al.* (2007, 2009). The choice of a dam-break event as a comparison term for the mathematical models should be able to point out the limits of the SWE assumption. Theoretically SWEs may not be suitable as a basis for a numerical model for violent wave overtopping or dam-break flow, where vertical velocities are a major feature and the SWE assumption is no longer valid. However, many researchers over the past years have used the shallow water model for numerical simulations (see e.g. Quecedo & Pastor (2002) for horizontal beds and Quecedo *et al.* (2004) for inclined beds). The SWE approach is successful due to its easy implementation and computational efficiency. Nevertheless, it is necessary to analyse the limitations of the SWE model when simulating flows with strong inertial effects and high free-surface gradients.

In this paper, we describe the mathematical models and their numerical discretization in § 2. Since two distinct numerical methods are involved, one based on the Eulerian approach (the WENO FV scheme) and the other on the Lagrangian approach (the SPH scheme), we first solve the simple one-dimensional dam-break flow to assess how the choice of the numerical discretization influences the accuracy of the solution (see § 3). Afterwards, we focus on the experiment carried out in the hydraulic laboratory of the University of Trento and published by Fraccarollo & Toro (1995). The description of the laboratory set-up of the dam-break problem is given in § 4.1. The numerical results and the critical comparison with the laboratory data are given in § 4.2. To conclude, final remarks are presented in § 5.

2. Mathematical models and their discretization

2.1. *The three-dimensional compressible Navier–Stokes equations*

2.1.1. *Governing PDE*

The motion of a weakly compressible fluid can be accurately described by the compressible isentropic Navier–Stokes equations, i.e. without energy equation. The system of governing partial differential equations in three dimensions is given by

$$\frac{\mathrm{d}\rho}{\mathrm{d}t} = -\rho\nabla\cdot\boldsymbol{v}, \tag{2.1}$$

$$\frac{\mathrm{d}\boldsymbol{v}}{\mathrm{d}t} = \frac{1}{\rho}\nabla\boldsymbol{\sigma} + \boldsymbol{S}, \tag{2.2}$$

$$\frac{\mathrm{d}\boldsymbol{x}}{\mathrm{d}t} = \boldsymbol{v}. \tag{2.3}$$

Equations (2.1) and (2.2) are the mass and momentum balance in non-conservative form. Equation (2.3) updates the position of each infinitesimal fluid element of the continuum. The term $\mathrm{d}/\mathrm{d}t$ denotes the total (material) derivative that follows the motion of the fluid. The variables to update are the density ρ, the velocity, $\boldsymbol{v}$, and the position $\boldsymbol{x}$. The vector $\boldsymbol{S}$ represents the body forces per unit mass, and it typically consists of the gravity acceleration $\boldsymbol{g}$. Finally, the total stress tensor, $\boldsymbol{\sigma}$, is defined as follows:

$$\boldsymbol{\sigma} = -p\boldsymbol{I} + \boldsymbol{\tau}, \tag{2.4}$$

where p is the pressure, $\boldsymbol{I}$ is the unit tensor and $\boldsymbol{\tau}$ is the viscous stress tensor. For an ideal inviscid fluid the stress is independent of the deformation rate and (2.4)

https://doi.org/10.1017/S0022112010003599 Published online by Cambridge University Press

is reduced to $\boldsymbol{\sigma} = -p\boldsymbol{I}$. For viscous Newtonian fluids, the following linear stress–strain rate relationship has to be introduced in (2.4). It models the flow of weakly compressible viscous fluids within local thermodynamic equilibrium, for which the Stokes hypothesis is valid:

$$\boldsymbol{\sigma} = (-p + \mu'\nabla \cdot \boldsymbol{v})\boldsymbol{I} + 2\mu\boldsymbol{D}, \quad 3\mu' + 2\mu = 0, \tag{2.5}$$

where μ is the dynamic bulk viscosity of the liquid and the term $\boldsymbol{D}$ is the strain rate tensor, defined as $\boldsymbol{D} = 1/2[\nabla\boldsymbol{v} + (\nabla\boldsymbol{v})^{\mathrm{T}}]$. In the following applications, we assume an ideal inviscid fluid. This is justified due to the very low resistance that the smooth horizontal plane bottom exerts on the fluid flow. Furthermore, any boundary layer effects are negligible in the present dam-break problem, since the bulk flow is entirely governed by gravity and inertia.

To close the PDE system, an equation of state is required. We refer to the so-called Tait equation, derived from a relation proposed by Batchelor (1974) for water. It approximates the liquid as a weakly compressible fluid and provides the relative pressure field, assuming the atmospheric reference pressure to be null,

$$p = k_0\left(\left(\frac{\rho}{\rho_0}\right)^{\gamma} - 1\right), \tag{2.6}$$

where ρ_0 is the reference fluid density at atmospheric pressure, and the exponent, γ, is a constant and usually set as $\gamma = 7$. The coefficient, k_0, determines the speed of sound, and it is taken so that the density fluctuations in the fluid flow $\delta\rho$ are sufficiently small by choosing a characteristic Mach number, M, of about $M \approx 0.1$ during the whole simulation. In this way, the density variations are consistent with the incompressible fluid assumption.

2.1.2. *Smooth particle hydrodynamics scheme*

The SPH method is a meshless scheme based on the Lagrangian approach. The fluid is discretized by a finite set of moving observation points, the so-called particles. To each SPH particle, the physical and kinetic properties of the fluid are assigned, such as density, pressure and velocity. The three-dimensional SPH method used in this study was recently proposed in Ferrari *et al.* (2009) and Ferrari (2009). In the momentum-conservation law, the flux given by the acoustic pressure waves is implemented resorting to a pure non-diffusive central flux, since there is no preferred direction for the propagation of pressure waves in subsonic flows. Instead, an upwind Rusanov-type flux in discrete form is used for the density equation. This numerical discretization recalls the advection upstream splitting method, developed by Liou & Steffen (1993) in the finite-volume framework. As proved by Ferrari *et al.* (2009); Ferrari (2009), monotone density fields as well as a monotone pressure distribution are computed using this new SPH scheme. It is stabilized by the implicit numerical viscosity that is given by the upwind Rusanov-type flux and based on the underlying Riemann problem. Moreover, a further improvement in the linear stability as well as the numerical accuracy is achieved by applying an explicit third-order total variation diminishing (TVD) Runge–Kutta time-integration scheme.

We underline that the SPH method used in this paper is completely free of any tunable numerical parameters, in contrast to other standard SPH algorithms found in the literature, such as the SPH method discussed in Monaghan (1994) which requires a careful calibration of an artificial viscosity term that bears no relation to real viscosities, but is designed to stabilize its numerical algorithm. Moreover, no kernel

https://doi.org/10.1017/S0022112010003599 Published online by Cambridge University Press

corrections, such as the moving least-squares kernel or the density re-initialization, have been used, which are very expensive from the computational point of view.

For the smoothing kernel function, W, which is typical of the SPH approach, we use the cubic B-spline kernel of Monaghan & Lattanzio (1985):

$$W_{ij} = \frac{C_\nu}{l^\nu} \begin{cases} \frac{2}{3} - q^2 + \frac{1}{2}q^3, & \text{if } 0 \leqslant q < 1, \\ \frac{1}{6}(2-q)^3, & \text{if } 1 \leqslant q < 2, \\ 0, & \text{if } q \geqslant 2, \end{cases} \tag{2.7}$$

where l is the so-called smoothing length and ν denotes the number of space dimensions. The normalization constant, C_ν, is chosen such that the integral over the kernel in the domain R^ν is equal to unity, i.e. $\int W \, \mathrm{d}V = 1$. In the three-dimensional case ($\nu = 3$), we have $C_\nu = 3/2\pi$. The dimensionless variable q is defined as

$$q = \frac{|\boldsymbol{x}_j - \boldsymbol{x}_i|}{l}, \tag{2.8}$$

where the vector $\boldsymbol{x}_j$ denotes the space position of the jth particle.

The semi-discrete SPH scheme according to Ferrari *et al.* (2009) is then written as follows:

$$\frac{\mathrm{d}\rho_i}{\mathrm{d}t} = -\sum_{j=1}^{N} m_j \left((\boldsymbol{v}_j - \boldsymbol{v}_i) \cdot \nabla_i W_{ij} - \boldsymbol{n}_{ij} \cdot \nabla_i W_{ij} \left(\frac{c_{ij}}{\rho_j} (\rho_j - \rho_i) \right) \right), \tag{2.9}$$

$$\frac{\mathrm{d}\boldsymbol{v}_i}{\mathrm{d}t} = -\sum_{j=1}^{N} m_j \left(\frac{p_i}{\rho_i^2} + \frac{p_j}{\rho_j^2} \right) \nabla_i W_{ij} + \boldsymbol{g}, \tag{2.10}$$

$$\frac{\mathrm{d}\boldsymbol{x}_i}{\mathrm{d}t} = \boldsymbol{v}_i, \tag{2.11}$$

$$p_i = k_0 \left(\left(\frac{\rho_i}{\rho_0} \right)^\gamma - 1 \right), \tag{2.12}$$

where m_j denotes the mass of the particle j. The operator ∇_i refers to differentiation with respect to the coordinate $\boldsymbol{x}_i$, i.e. $\nabla_i = \partial/\partial \boldsymbol{x}_i$. The equations above discretized (2.1)–(2.3) and (2.6). The term c_{ij} denotes the maximal celerity between the two interacting particles i and j

$$c_{ij} = \max(c_i, c_j), \quad c_i = \sqrt{\gamma \frac{k_0}{\rho_0} \left(\frac{\rho_i}{\rho_0} \right)^{(\gamma-1)}}. \tag{2.13}$$

We remark that introducing the Rusanov-type flux in the density equation corresponds to the introduction of an explicit penalty term for density jumps. This penalization of density fluctuations is consistent with the physics of nearly incompressible flow, where the density variations should tend to zero, however, as the Mach number tends to zero.

A major advantage of the SPH approach over classical finite-volume or finite-difference methods is the automatic treatment of the free-surface boundary condition, which is intrinsically satisfied. This follows from the equation of state (2.12), which evaluates the relative pressure field so that the atmospheric pressure is zero, in combination with the kernel interpolation, which does not produce any contributions to the flux from parts of the computational domain without interpolation points. Concerning the treatment of the solid boundaries, special care is required. In this study,

https://doi.org/10.1017/S0022112010003599 Published online by Cambridge University Press

the boundary conditions are imposed replacing the solid interfaces with boundary particles, following Ferrari *et al.* (2009). Each of the boundary elements interacts with all adjacent fluid particles by setting for each fluid particle a fictitious fluid point via local point symmetry. Finally, the boundary interactions are then added in summation form in conservation laws (see Ferrari *et al.* 2009 and Ferrari 2009 for more details).

2.2. *The two-dimensional depth-averaged shallow water equations*

2.2.1. *Governing PDE*

The two-dimensional depth-averaged SWEs are derived from (2.1) and (2.2) by integration in the z-direction using the assumptions that the fluid is incompressible and the characteristic horizontal length scale of the flow is much greater than the characteristic vertical length scale. This leads to neglect of any acceleration in the direction of gravity, yielding a hydrostatic pressure distribution in water. The resulting hyperbolic system of the governing partial differential equations is the well-known SWEs, written in the conservation form as

$$\frac{\partial W}{\partial t} + \nabla \cdot \boldsymbol{F} = 0, \tag{2.14}$$

where the vector of conserved variables, W, and the flux tensor, $\boldsymbol{F}$, are defined as

$$W = \begin{pmatrix} h \\ hu \\ hv \end{pmatrix}, \quad \boldsymbol{F} = \begin{pmatrix} hu & hv \\ hu^2 + \bar{p} & huv \\ huv & hv^2 + \bar{p} \end{pmatrix}, \quad \bar{p} = \frac{1}{2} g h^2, \tag{2.15}$$

where g is the gravitational constant, h is the water depth and u and v are the two horizontal velocity components. The system (2.14) can admit discontinuities into the solution.

2.2.2. *Unstructured weighted essentially non-oscillatory finite-volume scheme*

The numerical method used to solve the SWEs is an unstructured WENO finite-volume scheme of third order of accuracy in space and time, described in detail in Dumbser & Käser (2007) and Dumbser *et al.* (2007, 2008), where the order of accuracy property of the scheme was also verified. Here, we only summarize the main ideas. First, the computational domain Ω is divided into non-overlapping conforming triangles T_i, so that $\Omega = \cup T_i$. The method is then formulated as a one-step predictor–corrector method that is composed of the following three steps.

(i) Use a high-order accurate nonlinear WENO reconstruction. From the reconstruction procedure, one obtains the higher-order element-wise WENO reconstruction polynomials $w(\boldsymbol{x}, t^n)$ within each spatial cell at the current time t^n from the given cell averages $\bar{U}_i^n$, defined as follows:

$$\bar{U}_i^n = \frac{1}{|T_i|} \int_{T_i} U(\boldsymbol{x}, t^n) \, \mathrm{d}V. \tag{2.16}$$

Throughout this paper, we use the third-order version of the scheme. The WENO polynomials are obtained by a nonlinear weighting procedure,

$$w(\boldsymbol{x}, t^n) = \sum_s \omega_s w^s(\boldsymbol{x}, t^n), \tag{2.17}$$

of several reconstruction polynomials, $w^s(\boldsymbol{x}, t^n)$, each of them being obtained from a reconstruction over a different stencil, $\mathscr{S}_i^s$, in order to assure monotonicity at

https://doi.org/10.1017/S0022112010003599 Published online by Cambridge University Press

discontinuities. The nonlinear weights, ω_s, sum to unity, and the larger the nonlinear weights the smoother the reconstruction polynomial. Each individual polynomial, $w^s(\boldsymbol{x}, t^n)$, is obtained by requiring conservation for each element in the stencil, $\mathscr{S}_i^s$, as follows:

$$\frac{1}{|T_j|}\int_{T_j} w^s(\boldsymbol{x}, t^n)\,\mathrm{d}V = \bar{U}_j^n \qquad \forall\ T_j \in \mathscr{S}_i^s. \tag{2.18}$$

This (typically over-determined) equation system is solved by a constrained least-squares approach, where the linear constraint is that (2.18) is satisfied exactly at least in the element, T_i (see Dumbser & Käser 2007 and Dumbser *et al.* 2007 for more details).

(ii) The element-local predictor for each triangle, T_i, is computed by an element-local space–time Galerkin method which uses the WENO polynomials $w(\boldsymbol{x}, t^n)$ as the initial condition of a 'local Cauchy problem' of PDE (2.14) in order to construct for each element a local solution of the PDE, denoted by $\mathscr{W}_h = \mathscr{W}_h(\boldsymbol{x}, t)$ in the following. This means that one obtains the temporal evolution of the WENO reconstructed polynomial data inside each element, T_i, during one time step by solving an element-local weak formulation of the governing PDE (see Dumbser *et al.* 2009 for more details).

(iii) Update the cell averages, $\bar{u}_i^n$, to the next time level with a standard finite-volume scheme, i.e. compute $\bar{u}_i^{n+1}$ by

$$\bar{u}^{n+1} = \bar{u}^n - \frac{1}{|T_i|}\int_{t^n}^{t^{n+1}}\int_{\partial T_i} \mathbf{G}_{i+1/2}(\mathscr{W}_h^-, \mathscr{W}_h^+)\cdot\boldsymbol{n}\,\mathrm{d}S\,\mathrm{d}t, \tag{2.19}$$

where $\mathscr{W}_h^-$ denotes the boundary extrapolated data of the element-local space–time predictor from within elements T_i, and $\mathscr{W}_h^+$ denotes the boundary extrapolated data of the local space–time predictor from the neighbours, respectively. For the intercell flux $\mathbf{G}_{i+1/2}$, we use the recently proposed centred force method on general unstructured meshes of Toro, Hidalgo & Dumbser (2009).

3. One-dimensional dam-break problem

The following test case consists of a one-dimensional dam-break problem over a horizontal dry bottom, proposed by Stansby, Chegini & Barnes (1998), which investigated the initial stages just after the water release. At the initial conditions, still water with a depth, h_0, of 0.1 m is set in a tank of length 1.5 m. The experiments of Stansby *et al.* (1998) showed some jet-like phenomena just after the release and no wave breaking occurred. The jet interacts with the bed entraining air. At large times, a steady free-surface profile is achieved. Although in practice the release of water is not instantaneous but gradual, and the free-surface profile depends on water–soil interaction or concrete fracture at a breach, we omit simulation of these noises in the flow, according to Stansby *et al.* (1998).

The classical descriptions of the dam-break flows were obtained by Ritter (1892) and Stoker (1957). Their study led to the definition of two simple non-trivial solutions of the SWEs, and according to Gratton & Vigo (1994) they may also be interpreted as a limiting form of constant-flux gravity current. They are not of merely mathematical interest, because according to the study of Stansby *et al.* (1998) they provide a reasonably good description of the flow once transients associated with the initial release have died down. More recently, exact solutions for suspended sediment

https://doi.org/10.1017/S0022112010003599 Published online by Cambridge University Press

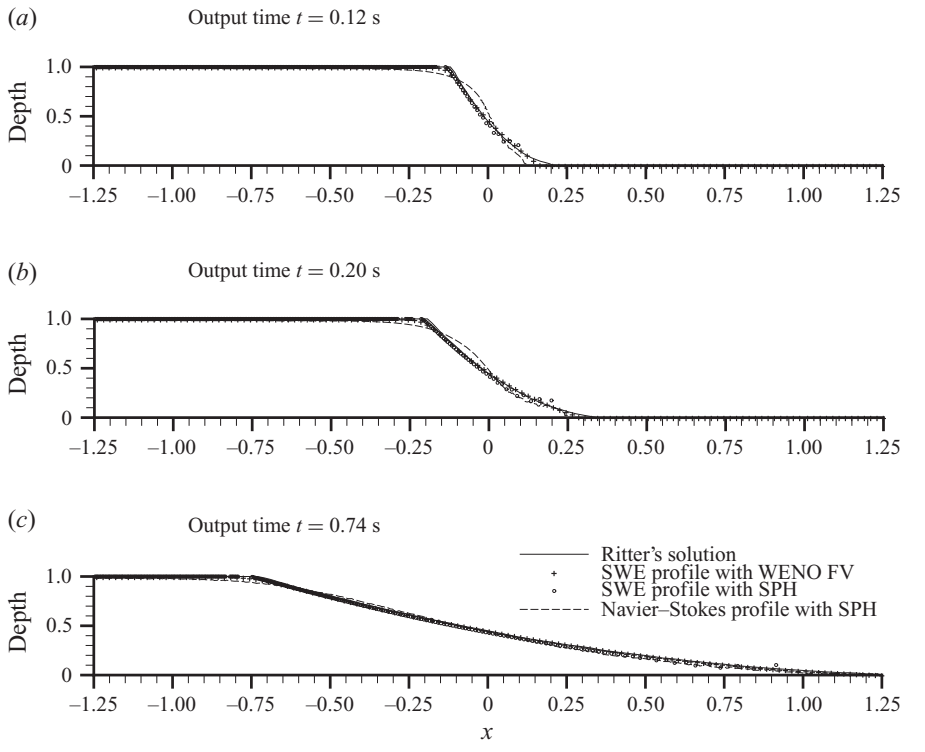


FIGURE 2. Analytical and numerical profiles of the free surface for a sequence of times, namely $t = 0.12$, 0.20 and 0.74 s. The water depth is normalized by h_0, that is, the initial height of the still water in the tank.

transport under one-dimensional dam-break flow, both over a dry bed and into a small water depth in front of the gate, have been computed by Pritchard & Hogg (2002). The analytical solution of Ritter (1892) refers to the dam-break flow over a dry horizontal bed. The flow field consists of an expansion wave, analogous to a rarefaction wave in gas dynamics, as follows:

$$h(x,t) = \frac{1}{9}\left(2 - \frac{x}{t}\right)^2, \quad v(x,t) = \frac{2}{3}\left(1 + \frac{x}{t}\right), \quad -1 \leqslant \frac{x}{t} \leqslant 2, \tag{3.1}$$

where t denotes the time coordinate with the origin defined as the instant when the gate leaves the bed, x is the space coordinate with the origin located at the exit, h represents the water depth and v is the velocity. Stoker's extension to Ritter's dam-break solution describes the propagation of a dam-break wave into a region of still water, i.e. $h > 0$ in front of the gate. Stoker's solution consists of a bore propagating into the water downstream of the exit, behind which is a region of uniform flow, the so-called 'star region'.

Numerical solutions are computed by applying the Lagrangian SPH discretization for both models, namely the Navier–Stokes equations and the shallow water approach. Moreover, the Eulerian discretization of the third-order WENO finite-volume scheme is used to solve the SWE model. A mesh size of 0.005 m is set for all computations. The analytical and numerical results are plotted in figure 2 for a sequence of times, namely

https://doi.org/10.1017/S0022112010003599 Published online by Cambridge University Press

$t = 0.12$, 0.20 and 0.74 s. They show the free-surface profiles and the y-coordinate for the depth is normalized by h_0, the initial water height in the tank. The SWE profiles computed by the SPH scheme and the third-order FV method agree well with each other and with the analytical Ritter solution at all output times. Good resolution is provided by both schemes, even if better accuracy is achieved by the FV method due to the high order. The front moves forwards from the exit producing a smooth flood wave that propagates like a bore upstream in the reservoir. According to Quecedo *et al.* (2005), the flooding tip velocity calculated using the shallow water approach is higher than the corresponding value calculated by the Navier–Stokes approach. Indeed, up to 0.20 s the flood wave arrival time of the Navier–Stokes solution does not coincide with that predicted by the SWE model. This is due to the local inertial effects in the vertical direction, which are neglected by the SWE assumption and delay the flooding propagation onto the dry bed. Then, the larger SWE value of the longitudinal velocity results in smaller arrival times of the water tip to a particular location.

Close to the breach site during the initial instants up to 0.20 s, the centre of curvature of the Navier–Stokes free surface is located below the free surface, contrary to the prediction of the SWE model. Then, the Navier–Stokes free-surface curvature changes its sign. Finally, as time evolves, the differences in the free-surface profiles between the SWE model and the Navier–Stokes approach reduce to become negligible. In figure 2 at the last output time $t = 0.74$ s, a rarefaction wave is also computed when the Navier–Stokes model is used. This is also confirmed by the laboratory experiments of Rouse (1950) and Stansby *et al.* (1998), which show good agreement between the experimental depression wave propagating into the reservoir and the shallow water theory for the one-dimensional dam-break problem. Similar observations can be drawn even when the dam-break flow includes the advance over a triangular obstacle, as proved by Goutal & Maurel (1997). Nevertheless, a discontinuity in the rarefaction wave is computed using the SWE approach, even at large times. We refer to the leading edge that propagates upstream in the reservoir. This high free-surface gradient consists of an artefact of the SWE model, because the experimental profile as well as the Navier–Stokes solution shows a smooth water depth variation.

From the comparison of the results, we can state that by applying the same SPH discretization to different models, namely the SWEs and the Navier–Stokes approach, a completely different solution is obtained. On the contrary, the free-surface profile computed by the Lagrangian mesh-free SPH scheme converges to that obtained by the Eulerian WENO FV method, when both approaches solve the same SWE model. This encourages us to continue our analysis on three-dimensional dam-break problems in order to investigate the applicability of the SWE approach for modelling such events and gives reasons for not choosing an analogous numerical discretization for both models, but comparing the SPH computations from the Navier–Stokes model with the WENO FV results from the SWEs in the following.

4. Three-dimensional dam-break problem

In the following, a three-dimensional dam rupture is simulated. Experimental measurements are available in the literature by Fraccarollo & Toro (1995). The laboratory data are used to validate the mathematical models, namely the SWEs and the Navier–Stokes approach. First, the experimental set-up plotted in figure 3 is briefly described. Afterwards, remarks and comments about the results are provided.

https://doi.org/10.1017/S0022112010003599 Published online by Cambridge University Press

Position	0	1	2	3	4	−5A	−4A	−3A	−2A	−1A
x (m)	0	0	0	0	0	−0.82	−0.62	−0.42	−0.22	−0.02
y (m)	0	0.04	0.08	0.12	0.16	0	0	0	0	0
Position	1A	2A	3A	4A	5A	6A	7A	8A	9A	10A
x (m)	0.02	0.12	0.222	0.322	0.422	0.522	0.622	0.722	0.822	1.022
y (m)	0	0	0	0	0	0	0	0	0	0
Position	11A	12A	13A	−4B	−3B	−2B	−1B	1B	2B	3B
x (m)	1.27	1.52	1.77	−0.845	−0.67	−0.323	−0.148	0.107	0.194	0.28
y (m)	0	0	0	−0.5	−0.4	−0.2	−0.1	0.05	0.1	0.15
Position	4B	5B	6B	7B	8B	9B	10B	11B	12B	C
x (m)	0.366	0.454	0.541	0.62	0.716	0.802	1.081	1.235	1.45	−0.495
y (m)	0.2	0.25	0.3	0.35	0.4	0.45	0.575	0.7	0.825	−0.65

TABLE 1. Table of the coordinates of each probe located on the plane bottom.

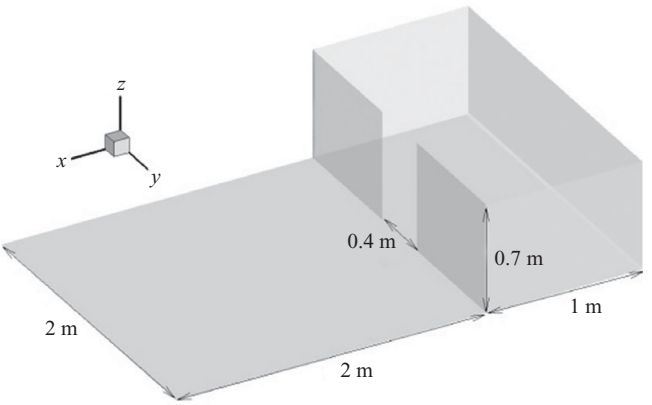


FIGURE 3. Schematic diagram of the laboratory device in three dimensions.

4.1. *Experimental set-up*

The laboratory set-up consists of a tank connected to a rectangular plate. It is built up of perspex sheets. The tank is 2 m wide and 1 m long with a rectangular exit. Still water in the tank is assumed at initial conditions with a depth equal to 0.6 m. The gate and the mechanism to open it are completely separated from the flume to avoid any noise in the laboratory measurements, such as high-frequency vibrations on the plane. The system guarantees a satisfactory waterproof closure and ensures the opening in a very short lapse of time, less than 0.1 s, through the rotation of the gate on a fixed hinge. Downstream of the gate, the flume consists of a dry horizontal plate 2 m long and 2 m wide. Open boundaries are set and the water overflows. A three-dimensional view of the laboratory set-up used by Fraccarollo & Toro (1995) is shown in figure 3.

After the release, the water front propagates downstream on the horizontal plane bottom and overflows at the open boundaries on all three sides (see figure 3). Experimental measurements have been provided by Fraccarollo & Toro (1995) at 40 gauges located in the tank and downstream along the plane bottom. Table 1 reports the coordinates of the gauges and a view in the x–y plane is plotted in figure 4. The data acquisition refers to the free-surface depth, the pressure value and the velocity

https://doi.org/10.1017/S0022112010003599 Published online by Cambridge University Press

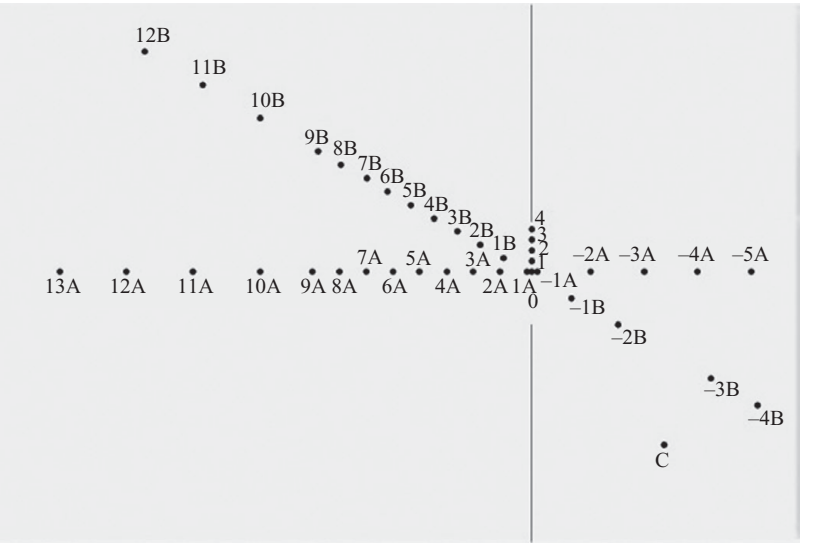


FIGURE 4. Schematic diagram in the x–y plane of the laboratory set-up with the location of the gauges.

field. The depth and pressure data are obtained using wave meters, which consist of a pair of nickel or chrome wires with a diameter of 0.3 mm, parallel to each other and 10 mm apart. They are linked to an electric circuit to measure the electric conductivity of water between the wires. Since the conductivity of water strongly depends on temperature and salt concentration, an initial calibration of the physical parameters of the still water in the reservoir is required. The velocity component along the longitudinal direction is measured employing a four electromagnetic velocity meter designed by the Delft Laboratory of Hydraulics. It works in the range of 0–2.5 m s^{-1} with an instrumental accuracy degree of ± 1 %. It provides a good spatial resolution, since the sensor is an ellipsoidal disk of 30 mm in diameter.

The data acquisition lasts for a period of 10 s. After that time, the water flow slowly varies and reaches the quasi-steady state with a hydrostatic pressure distribution almost everywhere.

4.2. *Comparison of the numerical results and the experimental data*

The numerical solutions have been computed applying the mathematical models described in § 2, i.e. the quasi-incompressible Navier–Stokes equations, solved using the three-dimensional SPH scheme of Ferrari *et al.* (2009) and the shallow water approach, solved using the third-order WENO finite-volume scheme of Dumbser *et al.* (2007). The SPH computation was run solving 600 000 fluid particles on 130 CPUs, whereas the results of the third-order WENO finite-volume scheme was obtained on an unstructured mesh of 62 294 triangular elements with a typical mesh spacing of $h = 0.01$. More computational effort is required by the SPH method to simulate the same test case. This lies on the intrinsic meshless nature of the SPH scheme, that requires a dynamic research of the neighbourhood for each particle at each time step, but it also depends on the choice of the mathematical model, i.e. the fully three-dimensional weakly compressible Navier–Stokes equations. Indeed, applying the depth-averaged integration of the Navier–Stokes equations to derive the well-known SWEs, we reduce the mathematical model to a two-dimensional approach. This clearly decreases not only the computational effort, but also the effectiveness of

https://doi.org/10.1017/S0022112010003599 Published online by Cambridge University Press

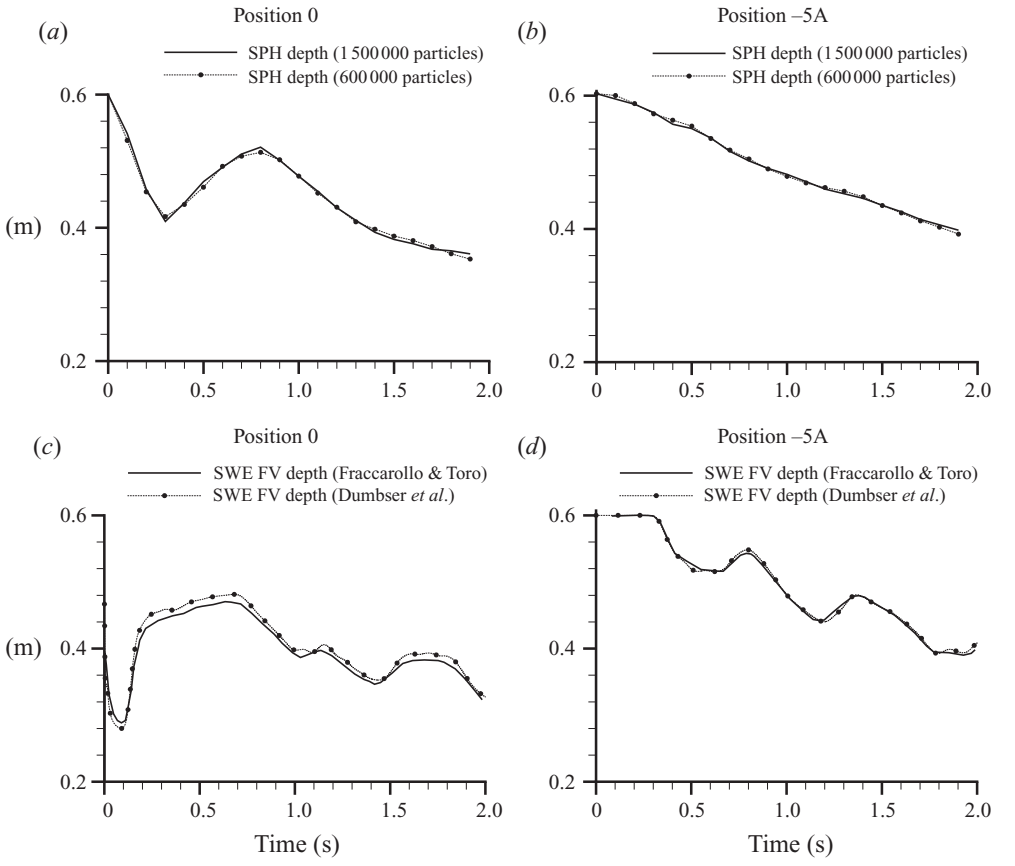


FIGURE 5. (a,b) Mesh convergence of the SPH solutions for the dam-break-type problem. (c,d) Comparison of the solutions computed with the third-order WENO FV scheme, proposed by Dumbser *et al.* (2007), on an unstructured mesh, against the numerical results provided by Fraccarollo & Toro (1995). The plots show the water depth up to 2 s.

the SWE model for reproducing physical phenomena. Then, since three-dimensional local inertial effects are completely lost in the SWE model, a comparison with the fully three-dimensional Navier–Stokes model and even the experimental data for a violent dam-break problem should be of interest due to the wide use of the SWEs in the scientific community.

In order to assess the convergence for the SPH solution, a mesh refinement was carried out. A computation with 1 500 000 particles to discretize the fluid volume in the tank was run. The results are plotted in figure 5(a,b). The plots show a comparison between the SPH results obtained using both refinements up to a time lapse of 2 s. They refer to the gauges 0 in figure 5(a,c), and -5 A in figure 5(b,d). For details on the gauge coordinates, see §4.1. From the comparison, the SPH solution computed using the rough discretization converges to the reference solution of 1 500 000 fluid particles. This proves that the fluid discretized by 600 000 SPH particles using an initial particle spacing of $h = \sqrt[3]{2} \times 10^{-2}$ is fine enough to preserve the desired degree of numerical accuracy. For a detailed convergence analysis in terms of the necessary number of SPH particles to discretize a flow feature, see Ferrari *et al.* (2009) and Ferrari (2010). In figure 5(a,c), the plots show the comparison of the SWE

https://doi.org/10.1017/S0022112010003599 Published online by Cambridge University Press

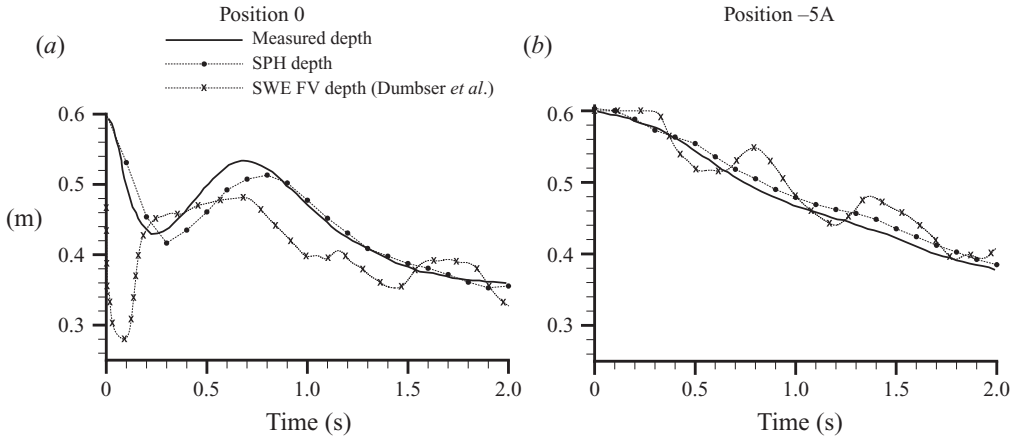


FIGURE 6. Plot of the the free-surface depth up to a time lapse of 2 s at gauge 0 (a) and -5 A (b). The SPH profiles are compared with the measurements and the third-order WENO FV solution.

profiles computed using the third-order WENO FV scheme against the numerical solution obtained by Fraccarollo & Toro (1995) on a regular mesh of 150 $\times$ 50 grid points. Their scheme consists of a two-dimensional shock-capturing technique to solve the SWE model that uses a second-order high-resolution TVD finite-volume method based on the weighted average flux method proposed by Toro (1992). A good agreement appears for both observation points, i.e. the gauges 0 and -5 A.

Now, we compare the numerical solutions given by the SPH scheme, which solves the Navier–Stokes approach, and the third-order WENO FV method, which solves the SWE model, against the experimental data at gauges 0 and -5 A. The panels in figure 6 show the results up to a time lapse of 2 s. Substantial deviations from the experimental measurements are apparent in the depth-averaged profiles predicted by the SWE model. This is especially evident in the initial stages of the dam-break flow: see figure 6(a). The plot shows the water depth at gauge 0, i.e. the observation point located at the exit. A marked underestimation of the free-surface elevation computed by the SWE model appears after the water release. The disagreement between the SWE signal and the measurements is given by the strong three-dimensional inertial effects of the flow, which are greater in the initial stage. They are completely neglected by the SWE model. As confirmed by the experimental observations of Fraccarollo & Toro (1995), the high free-surface gradient close to the gate produces a local non-negligible third component of acceleration, in the direction of gravity that has greater order of magnitude compared with the longitudinal velocity up to 0.5 s. Disagreement between the SWE profile and the experimental data appears at the gauge -5 A located in the reservoir (see figure 6b). Instead of a continuous monotone decrease of water depth, unphysical oscillations are computed from the SWEs from approximately 0.33 s. Indeed, a time delay after the removal of the gate until the first variation of the depth signal is received at gauge -5 A. We remark that this is a core point in our analysis. From the SWE model the gravity waves move with a finite-signal speed, equal to $\sqrt{gH}$, with H being the initial water height in the tank. In the specific case, the time delay can be estimated as $\Delta t = \Delta x/\sqrt{0.6g} \approx 0.33$ s, where Δx denotes the distance of the gauge -5 A from the exit. Otherwise, the weakly compressible Navier–Stokes model contains a much larger signal speed, given by the speed of sound $c \gg \sqrt{gH}$. For a perfectly incompressible medium, such as water in

https://doi.org/10.1017/S0022112010003599 Published online by Cambridge University Press

a subsonic regime, the Mach number M is equal to zero and the speed of pressure waves is infinitely high, so that the pressure signal produced by the opening of the gate reaches all the gauges immediately. This is consistent with the experimental observations. Using the Tait equation of state in the Navier–Stokes model, the fluid is assumed weakly compressible. Numerical experiments of Ferrari (2009) confirm that the density variations $\delta\rho$ are negligible, but consistent with the incompressible fluid assumption when a characteristic Mach number of $M \approx 0.1$ is set. Indeed, the maximum density fluctuations admitted is approximately $\delta\rho/\rho \approx M^{-2}$. Figure 6($a$,$b$) shows good agreement between the three-dimensional Navier–Stokes model and the measurements for the time-dependent free-surface evolution at both gauges. The reason lies in the completeness and suitability of the mathematical model. A small time lag between the Navier–Stokes signal and the measurements is shown at gauge 0 in figure 6(a). It is probably due to the assumption of negligible adherence phenomena and of an instantaneous water release, whereas in practice the gate removal is more gradual.

Figures 7 and 8 show the snapshots of the numerical results in the initial stages after the water release until a time lapse of $t = 2$ s. Interesting details can be detected from the comparison. As confirmed by the one-dimensional test case in § 3, the water front moves much faster when the SWEs are applied. This is derived from the SWE assumption of negligible acceleration component along the direction of gravity. The curvatures of the free surface at the exit are different. The rarefaction wave given by the SWE model moves with the centre of curvature located above the free surface. Instead, the centre of curvature in the Navier–Stokes solution is located below the free surface, but later on it changes sign and finally, as time evolves, this difference reduces to become negligible. The SWE approach predicts a wavy free surface in the reservoir, produced by the reflections on the tank walls of the depth-variation signal. The complex wave structure is fully developed after 2 s and it is sharply reconstructed due to the high order of accuracy of the WENO finite-volume scheme. Nevertheless, the wavy free surface in the tank is not confirmed by the experimental observations and the Navier–Stokes solution reproduces more accurately the monotone water depth decreasing in the reservoir. Some interesting results are also obtained when we focus on the front flooding downstream over the horizontal plate. At time $t = 0.5$ s, a longitudinal crest on the Navier–Stokes free-surface profile appears (see figure 7). This is in disagreement with the SWE solution. From the observation of the photograph in figure 9 related to the experiments, a similar shape on the free surface seems to appear. For more clarity, the black and white picture is reported where the contour lines are pointed out. The flood on the horizontal plate in front of the exit takes a spade-like shape. This is true using both mathematical models. The central stream of the flow is faster. The water progressively propagates laterally, but the walls adjacent to the gate are not immediately wet. A substantial validation comes from the qualitative comparison with the photograph of the experiments in figure 9.

Figure 10 shows the plots of the streamlines in the symmetric longitudinal-vertical plane computed using the Navier–Stokes model. Each plot refers to a specific time value, namely $t = 0.2$, 0.3, 0.4, 0.5, 1 and 2 s. Colours denote the Navier–Stokes pressure field. The bold line in black shows the water depth predicted by the SWE model. The streamlines, due to the strong unsteadiness, cross the free surface. It is particularly evident in the upstream reach.

The plots in figures 11 and 12 show the stage hydrographs (on the left) and the pressure values at the bottom (on the right). They report the experimental data of Fraccarollo & Toro (1995), the SWE results and the Navier–Stokes solution at gauges

https://doi.org/10.1017/S0022112010003599 Published online by Cambridge University Press

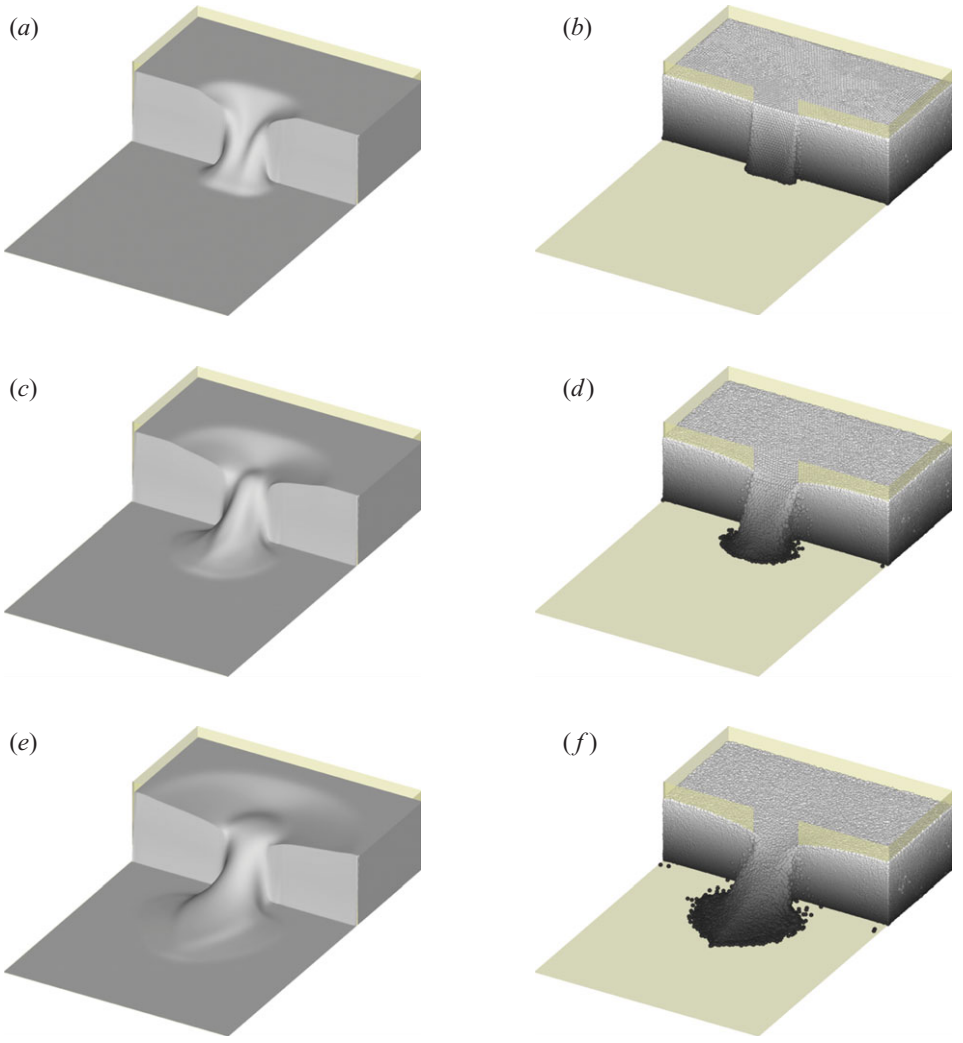


FIGURE 7. (Colour online) Initial stages of the three-dimensional dam-break phenomenon as computed by the third-order WENO finite-volume scheme using the SWE approach (a, c, e) and by the three-dimensional SPH method using the Navier–Stokes model (b, d, f). The snapshots refer to times $t = 0.1$, $t = 0.2$ and $t = 0.3$ s.

0, −5 A, −3 A, −2 A, 1 A, 8 A and 4, up to 10 s after the water release. After that the longitudinal flow is completely developed and the pressure distribution is hydrostatic at all gauges. Both mathematical models fit well in the steady flow condition. This confirms the validity of the SWE assumption at large times. Nevertheless, an extremely oscillating pressure field during the unsteady flow (approximately up to 4 s) is predicted by the SWE model with heavy deviations from the experimental data (see figure 11). This is true at all gauges. The Navier–Stokes solution reproduces the monotonous behaviour of the measurements in emptying the tank at all times, even during the unsteady stage. Good agreement with the experimental measurements is achieved by the Navier–Stokes model, even if a rapid artificial dip in the pressure evolution appears immediately after the water release. It is related to the Tait equation of state. An acoustic wave on the bottom propagates in the tank as soon as the gate is removed,

https://doi.org/10.1017/S0022112010003599 Published online by Cambridge University Press

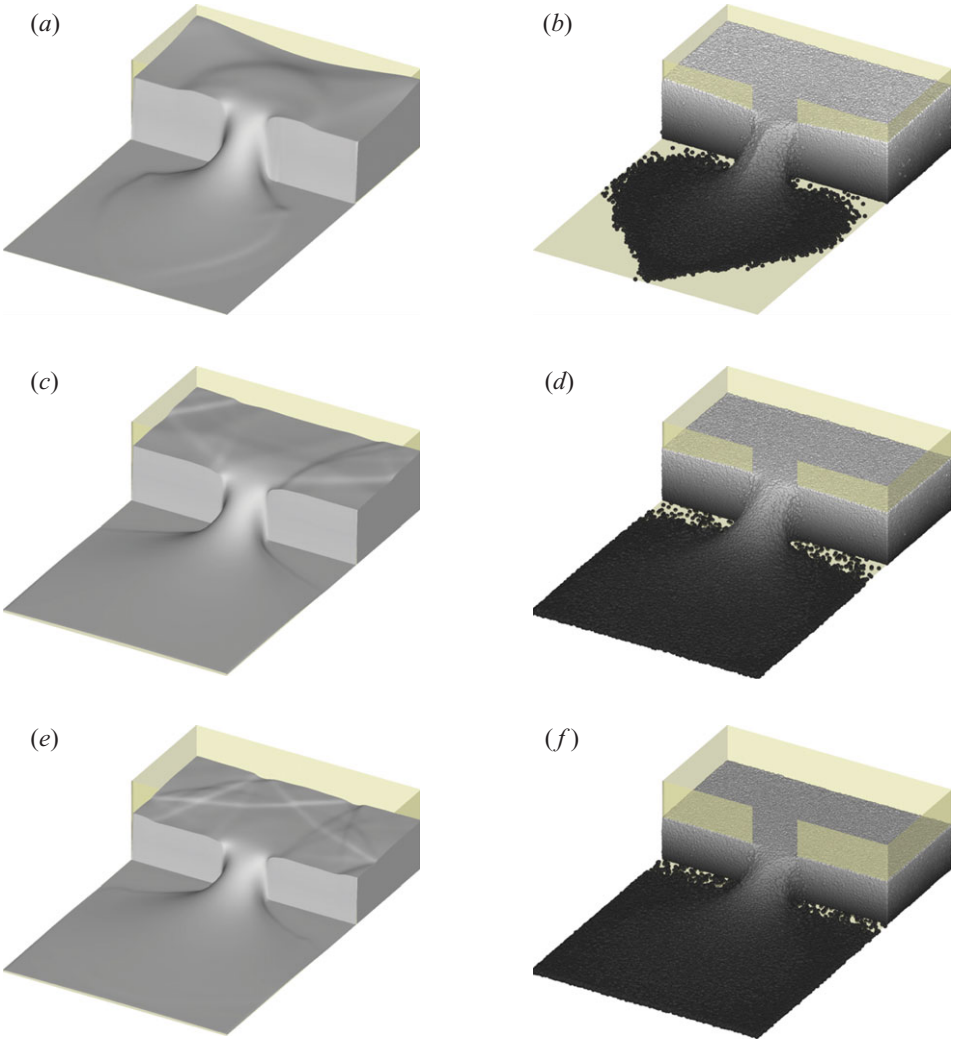


FIGURE 8. (Colour online) Initial stages of the three-dimensional dam-break phenomenon as computed by the third-order WENO finite-volume scheme using the SWE approach (a, c, e) and by the three-dimensional SPH method using the Navier–Stokes model (b, d, f). The snapshots refer to times $t = 0.5$, $t = 1$ and $t = 2$ s.

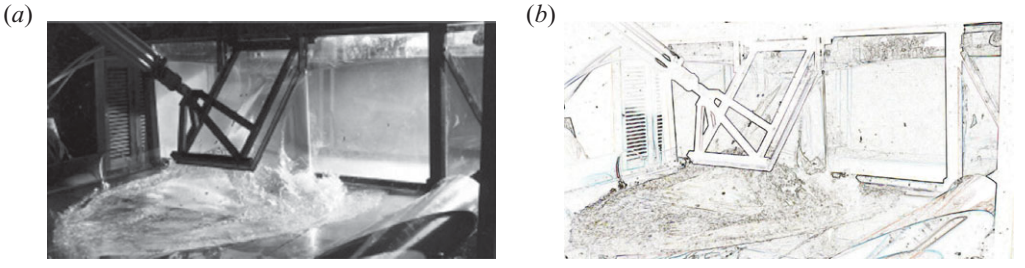


FIGURE 9. (Colour online) Photograph of the laboratory experiments carried out by Fraccarollo & Toro (1995). (a) Colour picture and (b) black and white picture.

https://doi.org/10.1017/S0022112010003599 Published online by Cambridge University Press

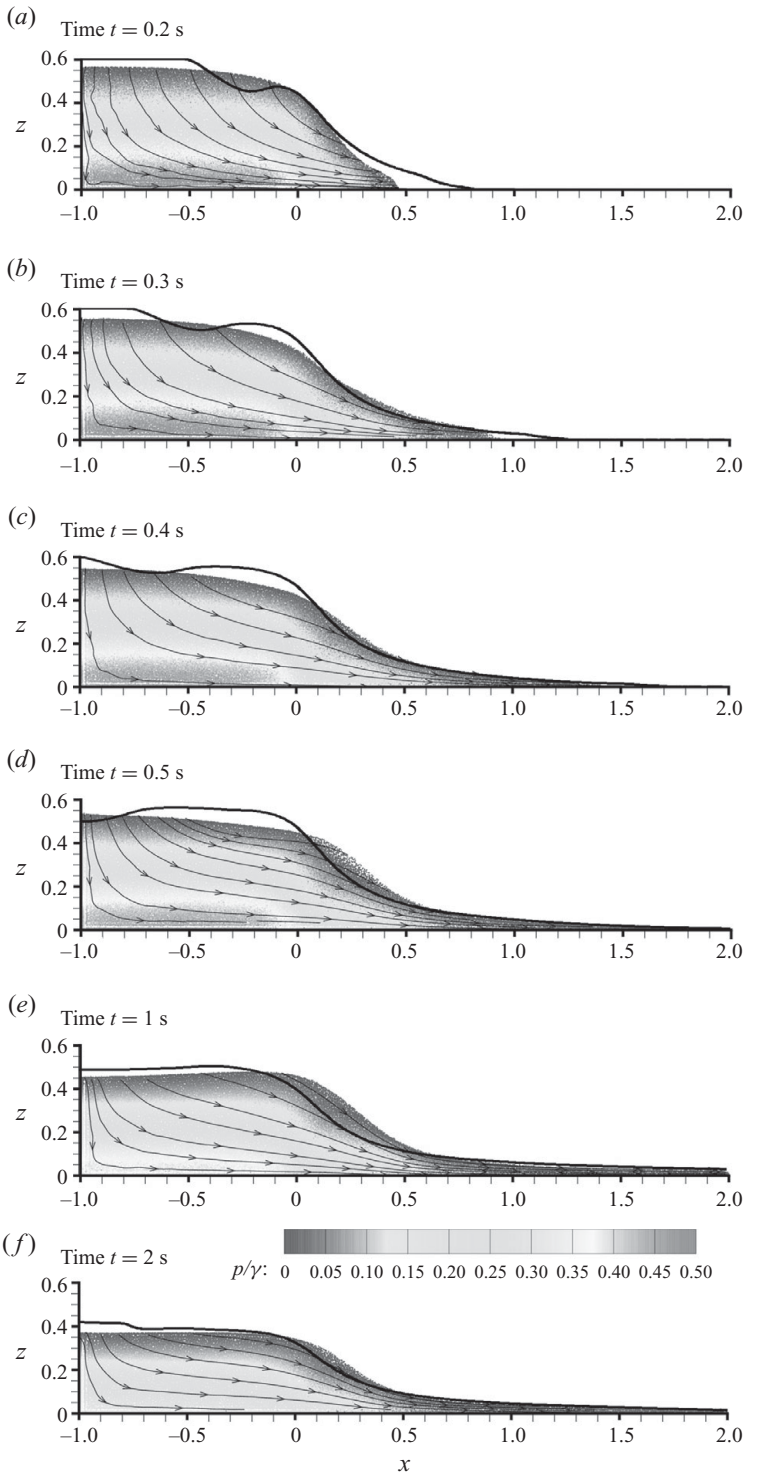


FIGURE 10. The streamlines (arrow line) and the pressure field (colours) computed using the Navier–Stokes model and the water depth (solid line in black) obtained using the SWE approach. The plots refer to time $t = 0.2$, $t = 0.3$, $t = 0.4$, $t = 0.5$, $t = 1$ and $t = 2$ s.

https://doi.org/10.1017/S0022112010003599 Published online by Cambridge University Press

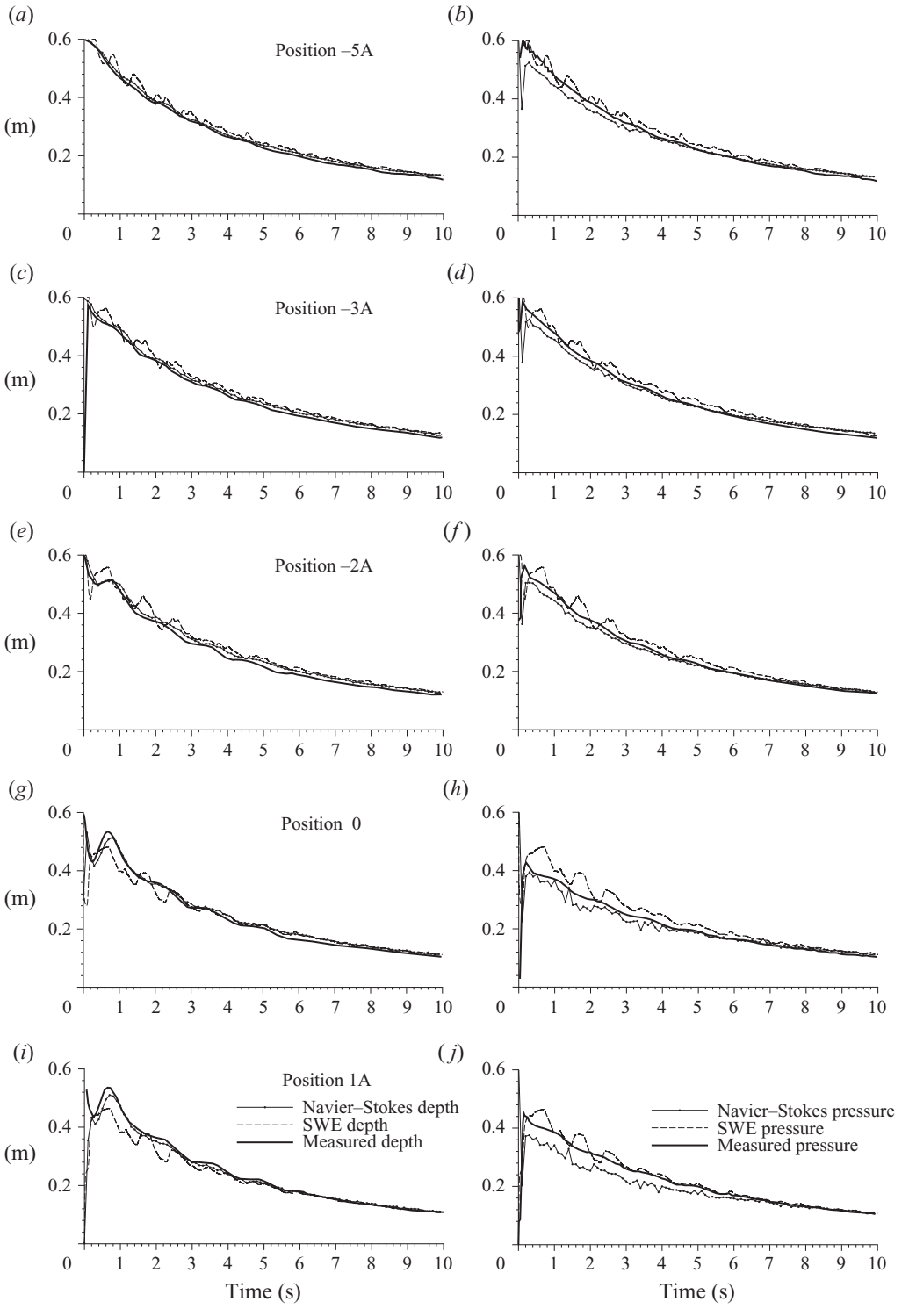


FIGURE 11. The Navier–Stokes depth (a, c, e, g, i) and pressure at the bottom (b, d, f, h, j) are compared against the experimental data and the SWE solution at gauges −5 A, −3 A, −2 A, 0 and 1 A.

https://doi.org/10.1017/S0022112010003599 Published online by Cambridge University Press

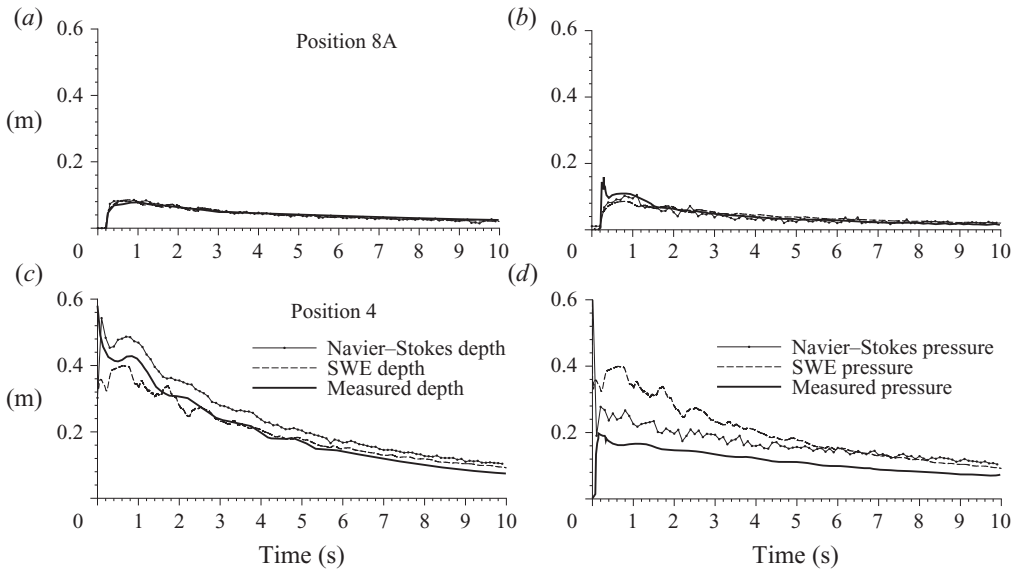


FIGURE 12. The Navier–Stokes depth (a, c) and pressure (b, d) are compared against the experimental data and the SWE solution at gauges 8 A and 4.

producing the noise in the pressure evolution. In the shallow water approach, the pressure distribution at the exit starts from the hydrostatic value, whereas in the Navier–Stokes solution it changes to zero after the instantaneous removal of the retaining wall. Close to the exit (gauges 0, 1 A and 4), significant deviations from the hydrostatic assumption are measured by Fraccarollo & Toro (1995), even up to 60 % higher than the hydrostatic during the first 2 s. Then, the SWE assumption is not valid close to the failure site in the initial stage. In particular, the closer the point to the failure site the larger the error and the longer it takes for the convergence of the SWE solution to the Navier–Stokes solution. After approximately 0.5 s, the depth measurement close to the exit (gauges 0, 1 A and 4) shows a rising stage due to the contribution of the lateral propagation of the flow. This is accurately reproduced by the Navier–Stokes solution as well as the alternating periods of quickly diminishing and frozen stages in the free-surface height. Instead, the strong free-surface oscillations predicted by the SWEs show the shortcomings of the mathematical model in predicting the initial stage of the dam-break flow. Nevertheless, it seems to have no influence on the SWE accuracy at large times.

Velocity measurements are provided by Fraccarollo & Toro (1995) at the positions 0, −5 A, −3 A and −2 A. They provide eight curves, each of them measured at a different height from the bottom. The gauges start at the level 50 mm up to level 0.4 m. A curve at every 50 mm has been provided with an ending time depending on the free-surface depth. Figure 13(a, d, g, j) shows the experimental velocity profiles. They achieve a maximum value after 0.5 s and decrease with an oscillating behaviour. The fluctuations correspond to the alternating descending and stationary phases of the free-surface signal (see figures 11 and 12). The frequency of the cycle is about 4/5 Hz. The velocity computed by the SWE model represents flow-depth-averaged values, and they are substantially different from the experimental data. Therefore, the SWE model fails to reproduce the flow-depth-averaged values of velocity. Otherwise, more accurate results are obtained from the fully three-dimensional Navier–Stokes

https://doi.org/10.1017/S0022112010003599 Published online by Cambridge University Press

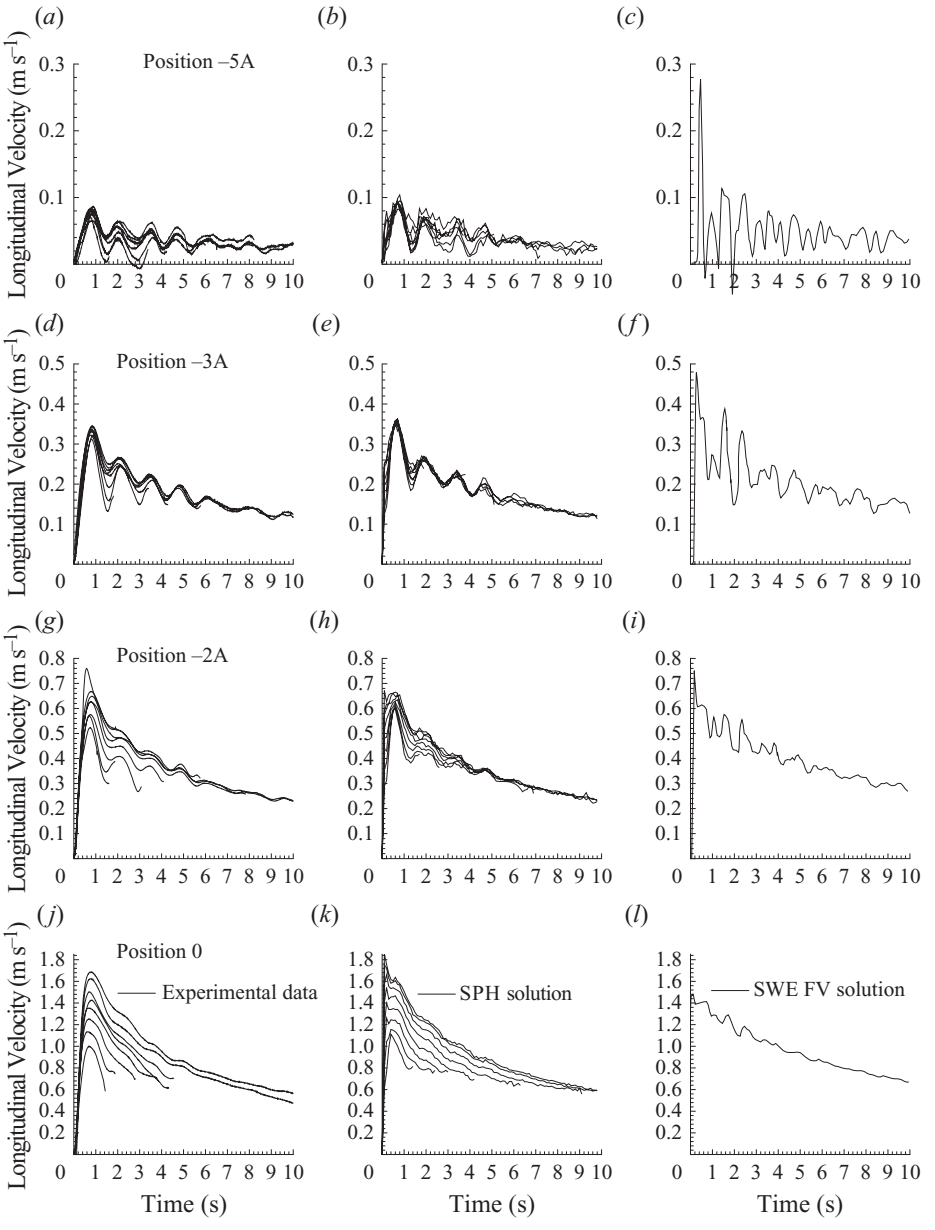


FIGURE 13. Velocity component in longitudinal direction at the gauges −5 A, −3 A, −2 A and 0. The Navier–Stokes solution is compared against the SWE results and the experimental data.

approach, achieving good agreement with the experiments at all gauges. According to Quecedo *et al.* (2005) during the first instants, basically up to the instant corresponding to the maximum of the pressure evolution, the vertical component of the velocity is of the same order as or larger than the horizontal component. The longitudinal velocity increases as time evolves to be, finally, the relevant one. Therefore, the SWE assumption of negligible acceleration in the vertical direction is valid only at large times, and the shallow water model can provide good performance.

https://doi.org/10.1017/S0022112010003599 Published online by Cambridge University Press

5. Conclusions

In this paper, an accurate investigation of dam-break problems has been carried out. Two mathematical models have been compared, namely the weakly compressible Navier–Stokes model solved by using the meshless SPH method proposed by Ferrari *et al.* (2009) and the classical SWEs solved by using the unstructured third-order WENO finite-volume scheme of Dumbser *et al.* (2007). Since negligible vertical accelerations are assumed when collapsing the three-dimensional Navier–Stokes equations to obtain the two-dimensional SWEs, the SWE model may not be suitable as a basis for a numerical model to simulate high free-surface gradient flows for such dam-break problems. Then, a critical analysis has been developed by comparing the SWE model against the weakly compressible Navier–Stokes approach and experimental measurements provided by Fraccarollo & Toro (1995). Based on our results, it can be concluded that the SWE model computes a faster propagation wave over a dry bed in the initial stage, thus anticipating the arrival time of the water front. It estimates reasonably well the evolution of the water depth far from the dam, but it completely miscalculates the evolution of the free-surface flow close to the gate during the initial stages when the free-surface curvature is high. This is due to the SWE assumption which results in a hydrostatic pressure distribution. Thus, the SWE model fails the pressure value in short time evolutions and should not be used for calculating, for instance, stresses on structures. Nevertheless, at large times the SWE model provides good performance. The fully three-dimensional Navier–Stokes equations predict with success the flooding evolution, as proved by the comparison against the experimental data, even during the first instants. However, the simple implementation and the computational efficiency of the SWE approach explains its very frequent application in the framework of geophysical applications or hydraulic, civil or environmental engineering, in spite of its shortcomings. Although much larger computational effort is required to solve the three-dimensional Navier–Stokes equations, the authors are of the opinion that the Navier–Stokes approach will be used more and more by the scientific community to simulate large-scale phenomena, thanks to the increasing computational power provided by the recent multiprocessor computers, and access to modern massively parallel supercomputers.

The work of A.F. was supported by the HPC Europe programme, carried out at the High Performance Computing Center Stuttgart (HLRS), Germany. M.D. acknowledges support by the Leibniz Rechenzentrum (LRZ), München, Germany.

REFERENCES

Batchelor, G. K. 1974 *An Introduction to Fluid Mechanics*. Cambridge University Press.

Dumbser, M., Balsara, D., Toro, E. F. & Munz, C. D. 2008 A unified framework for the construction of one-step finite-volume and discontinuous Galerkin schemes. *J. Comput. Phys.* **227**, 8209–8253.

Dumbser, M., Castro, M., Toro, C. & Pares E. F. 2009 ADER scheme on unstructured meshes for non-conservative hyperbolic equations: applications to geophysical flows. *Comput. Fluids* **38**, 1731–1748.

Dumbser, M. & Käser, M. 2007 Arbitrary high order non-oscillatory finite volume schemes on unstructured meshes for linear hyperbolic systems. *J. Comput. Phys.* **221**, 693–723.

Dumbser, M., Käser, M., Titarev, V. A. & Toro, E. F. 2007 Quadrature-free non-oscillatory finite volume schemes on unstructured meshes for nonlinear hyperbolic systems. *J. Comput. Phys.* **226**, 204–243.

Ferrari, A. 2009 *A New Smooth Particle Hydrodynamics Scheme for 3D Free Surface Flows*. VDI.

https://doi.org/10.1017/S0022112010003599 Published online by Cambridge University Press

Ferrari, A. 2010 SPH simulation of free surface flow over a sharp-crested weir. *Adv. Water Res.* **33**, 270–276.

Ferrari, A., Dumbser, M., Toro, E. F. & Armanini, A. 2009 A new 3D parallel SPH scheme for free surface flows. *Comput. Fluids* **38**, 1203–1217.

Fraccarollo, L. & Toro, E. F. 1995 Experimental and numerical assessment of the shallow water model for two-dimensional dam-break type problems. *J. Hydraul. Res.* **33**, 843–864.

Goutal, N. & Maurel, F. 1997 Proceedings of the second workshop on dam-break wave simulation. *Tech Rep*. HE-43/97/016/A. Electrité de France, Département Laboratoire National d'Hydraulique, Groupe Hydraulique Fluviale.

Gratton, J. & Vigo, C. 1994 Self-similar gravity currents with variable inflow revisited: plane currents. *J. Fluid Mech.* **258**, 77–104.

Liou, M.-S. & Steffen, C. 1993 A new flux splitting scheme. *J. Comput. Phys.* **107**, 23–39.

Monaghan, J. J. 1994 Simulating free surface flows with SPH. *J. Comput. Phys.* **110**, 399–406.

Monaghan, J. J. & Lattanzio, J. C. 1985 A refined particle method for astrophysical problems. *Astron. Astrophys.* **149**, 135–143.

Pritchard, D. & Hogg, A. J. 2002 On sediment transport under dam-break flow. *Fluid Mech.* **473**, 265–274.

Quecedo, M. & Pastor, M. 2002 A reappraisal of the Taylor–Galerkin algorithm for drying–wetting areas in shallow-water computations. *Intl J. Numer. Methods Fluids* **38**, 515–531.

Quecedo, M., Pastor, M., Herreros, M. I. & Merodo, J. A. F. 2004 Numerical modelling of the propagation of fast landslides using the finite element method. *Intl J. Numer. Methods Engng* **59**, 755–794.

Quecedo, M., Pastor, M., Herreros, M. I., Merodo, J. A. F. & Zhang, Q. 2005 Comparison of two mathematical models for solving the dam break problem using the FEM method. *Comput. Methods Appl. Mech. Engng* **194**, 3834–4005.

Ritter, A. 1892 Die Fortpflanzung der Wasserwellen. *Z. Verein. Deutsch. Ing.* **36**, 947–954.

Rouse, H. 1950 *Engineering Hydraulics*. Wiley.

Stansby, P. K., Chegini, A. & Barnes, T. C. D. 1998 The initial stages of dam-break flow. *J. Fluid Mech.* **374**, 407–424.

Stoker, J. J. 1957 *Water Waves: The Mathematical Theory with Applications*. Wiley Interscience.

Toro, E. F. 1992 Riemann problems and the WAF method for solving the two-dimensional shallow water equations. *Phil. Trans. R. Soc. Lond.* **338**, 43–68.

Toro, E. F., Hidalgo, A. & Dumbser, M. 2009 FORCE schemes on unstructured meshes. Part I. conservative hyperbolic systems. *J. Comput. Phys.* **228**, 3368–3389.

https://doi.org/10.1017/S0022112010003599 Published online by Cambridge University Press